NANO · MICRO small
www.small-journal.com

Effects of Unit Cell Size on Thermal Conductivity in Two Different Polymorphs of Niobium Diselenide

Sungjin Park, Kyomin Kim, Kwangrae Kim, Wooyoung Lee, Aloysius Soon, Jong-wook Roh,* and Woochul Kim**

2D materials possess weak inter-layer van der Waals bonding, allowing them to exist as different polymorphs depending on the stacking sequence of the layers. Herein, the thermal conductivities of the 2H-NbSe$_2$ and 2H-3R-NbSe$_2$ polymorphs by conducting experimental measurements and theoretical analysis are comparatively studied. Owing to its 1.8 times larger unit cell, 2H-3R-NbSe$_2$ has a considerably greater number of optical phonon branches than does 2H-NbSe$_2$, suggesting that 2H-3R-NbSe$_2$ absorbs thermal energy rather than transporting it. In addition, scattering is more likely to occur in 2H-3R-NbSe$_2$ because a far greater number of states satisfy the selection rule. As a result of these, the 2H-3R-NbSe$_2$ has considerably lower thermal conductivity than that of the 2H-NbSe$_2$. The results highlight how the size of the unit cell affects the thermal conductivities of polymorphs.

1. Introduction

Polymorphism in materials allows for the tuning of their electrical and thermal properties owing to their ability to exist in different crystal structures while maintaining the same chemical composition.[1] While theoretical analyses of changes in thermal conductivity due to polymorphism exist,[2–11] experimental data are scarce, except in the case of carbon-based materials,[12,13] such as diamond,[14] graphene,[15–17] graphite,[18,19] and carbon nanotubes,[20,21] and polymorphs of $Ge_2Sb_2Te_5$,[22] InAs nanowires,[23] and Cu_2SnS_3.[24] In fact, to our knowledge, a comparative study on the experimentally measured thermal conductivities of 2D transition metal materials and their polymorphs has not been reported thus far.

2D materials, especially 2D transition-metal dichalcogenides (TMDs), exhibit different properties compared to those of their bulk counterparts owing to weak inter-layer van der Waals bonding.[25–27] This weak bonding allows 2D materials to exist as different polymorphs depending on the stacking sequence of the layers.[28] Typical polymorphs are the 2H and 1T phases, which usually represent semiconducting properties and metallic properties, respectively.[29] Owing to such properties, 2D materials have unique electrical properties, and various studies have investigated representative 2D materials, such as MoS_2, WSe_2, and WTe_2.[28,30,31] In a recent work, Sun et al.[32] experimentally measured the thermal conductivity of 2H-NbSe$_2$ by interlayer decoupling of an aerogel-like superlattice consisting of highly porous hydroxide and NbSe$_2$ layers. This work showed that intrinsic 2D properties of bulk materials can be measured without mechanical exfoliation. In another work by Zhu et al.,[33] the thermal conductivity of a few-layer 2H-NbSe$_2$ sample was measured using the heat diffusion imaging method. Their measured maximum thermal conductivity value of 53 W mK^{-1} was much higher than that of bulk 2H-NbSe$_2$ reported in another work by Beletskii et al.[34] and revealed that phonons are the major heat carriers in few layer 2H-NbSe$_2$. This increase in thermal conductivity in extremely thin 2D materials may be attributed to the diminished effect of Umklapp scattering as only the boundary scattering of phonons becomes relevant to the thermal transport.[35] Additional works report low-temperature thermal conductivity of 2H-NbSe$_2$ to study the thermal transport at the superconducting state.[36,37] However, the thermal properties of 2D TMD materials and their polymorphs have not been experimentally measured thus far to the best of the author's knowledge, although a few theoretical analyses have been reported in the literature.[38–43]

Herein, a comparative study on the difference in the thermal conductivities of two polymorphs (2H- and 2H-3R polymorphs) of NbSe$_2$ (see **Figure 1a**) is determined by conducting experimental measurements and performing a theoretical analysis. NbSe$_2$ is a 2D TMD in which Se-Nb-Se forms a sandwich-like covalent

---

S. Park, K. Kim, W. Kim
School of Mechanical Engineering
Yonsei University
Seoul 03722, Republic of Korea
E-mail: woochul@yonsei.ac.kr

K. Kim
Texas Materials Institute and Department of Mechanical Engineering
The University of Texas at Austin
Austin, TX 78712, USA

W. Lee, A. Soon
Department of Materials Science and Engineering
Yonsei University
Seoul 03722, Republic of Korea
E-mail: aloysius.soon@yonsei.ac.kr

J.-wook Roh
School of Nano and Materials Science and Engineering
Kyungpook National University
Gyeongsangbuk-do 38869, Republic of Korea
E-mail: jw.roh@knu.ac.kr

The ORCID identification number(s) for the author(s) of this article can be found under https://doi.org/10.1002/smll.202408948

DOI: 10.1002/smll.202408948

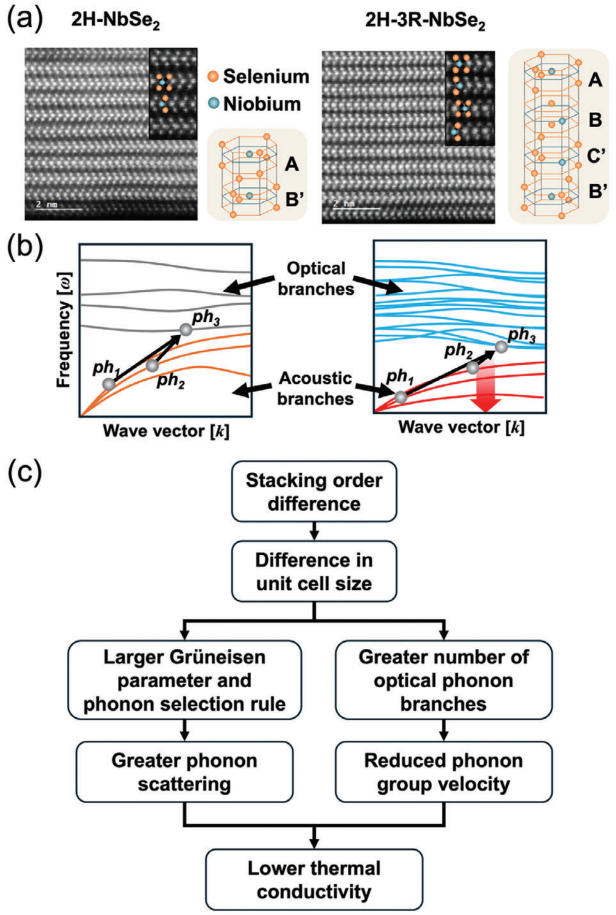

Figure 1. a) STEM images of 2H-NbSe$_2$ and 2H-3R-NbSe$_2$ showing differences in their stacking sequences. b) Effect of the enlarged unit cell on phonon branches and phonon scattering. c) The effect of stacking order difference on thermal conductivity of NbSe$_2$ and its polymorph.

bond. The 1H (hexagonal) monolayer NbSe$_2$ can form different phases, such as 2H, 4H, and 3R (rhombohedral), through van der Waals bonding. As with the well-studied MoS$_2$,[44] Moon et al.[45] reported that the unit cell volumes of 2H- and 2H-3R-NbSe$_2$ differ owing to differences in their stacking sequences. As illustrated in Figure 1b, the change in unit cell volume is expected to cause changes in the phonon group velocity and anharmonicity of these materials, resulting in the lower thermal conductivity of 2H-3R-NbSe$_2$. A larger unit cell leads to an increase in the number of optical phonon branches, which reduces the phonon group velocity.[46] Additionally, the aforementioned change in unit cell volume can affect the phonon selection rule and the Grüneisen parameter, which are related to phonon scattering.[47–49] Herein, we investigate the effect of changes in unit cell volume on the thermal conductivities of 2H- and 2H-3R-NbSe$_2$ (Figure 1c).

2. Materials and Methods

2.1. Material Synthesis and Characterization

Details in material synthesis[45] are available in the supporting information so only a brief summary is provided here. Niobium and selenium powders were weighed and mixed according to the stoichiometric ratio. After mechanical mixing with ethanol, the mixture was dried to vaporize the ethanol in the mixture. The dried mixture was then vacuum sealed in a quartz tube and heat treated to finally obtain 2H-3R-NbSe$_2$ samples. Reference 2H-NbSe$_2$ samples were purchased from HQ graphene.

Table 1. Lattice constants and unit cell volumes of 2H- and 2H-3R-NbSe$_2$.

	a [Å]	b [Å]	c [Å]	V [Å^3]
2H	3.422	3.422	12.169	142.26
2H-3R	3.412	3.412	24.547	260.41

To ensure that the as-synthesized samples were indeed 2H-3R-NbSe$_2$, material characterization was performed (Figure S1, Supporting Information). The crystal structures of the synthesized 2H-3R-NbSe$_2$ and 2H-NbSe$_2$ samples were observed with X-ray diffraction, and the observed peak locations agreed with that of the reference pattern reported in a previous study.[45] Further characterization using Raman spectroscopy analysis and X-ray photoemission spectroscopy was performed revealing the difference in stacking sequence and unchanged chemical state. All results were in agreement with the data presented in the reference work,[45] confirming the correct synthesis of 2H-3R-NbSe$_2$.

The structural characteristics of the synthesized 2H- and 2H-3R-NbSe$_2$ were confirmed through scanning transmission electron microscopy (STEM) imaging (see Figure 1a). To obtain STEM images, cross-sectional NbSe$_2$ samples were prepared using focused ion beam (FIB) milling. These samples were then transferred to the STEM to observe their layered structures. Figure 1a depicts a schematic diagram of the layered structure and STEM image of the 2H phase. The distributions of niobium (teal circle) and selenium (orange circle) in the inset STEM image are consistent with those in the schematic diagram. The schematic diagram of the layered structure and the STEM image of the 2H-3R phase are depicted in Figure 1a. Likewise, the distributions of niobium and selenium in the inset STEM image were consistent with those in the schematic diagram, indicating that the synthesized 2H-3R phase sample was indeed 2H-3R-NbSe$_2$. Additionally, density functional theory (DFT) optimized lattice constants of 2H-NbSe$_2$ and 2H-3R-NbSe$_2$ were obtained, as listed in **Table 1**, and these constants confirmed the 1.8 times larger unit cell volume of the 2H-3R-NbSe$_2$ resulting from differences in the stacking sequences. Such enlarged unit cells due to differences in stacking sequence are also evident in other 2D layered materials and their polymorphs such as MoS$_2$, TaS$_2$, and WSe$_2$ due to the weak van der Waals bonding between the layers.[44,50–54]

2.2. Thermal Conductivity Measurement

To measure the thermal conductivity of thin film NbSe$_2$, the previously synthesized bulk NbSe$_2$ samples were mechanically exfoliated to obtain thin films. These thin films were then randomly transferred onto a micro-fabricated measurement device by using a PDMS block. The micro-fabricated measurement device consisted of a heater suspended between two heatsinks, as illustrated in **Figure 2**a. The sample to be measured was placed between the heaters and a third heatsink to form a T-shape, which gives

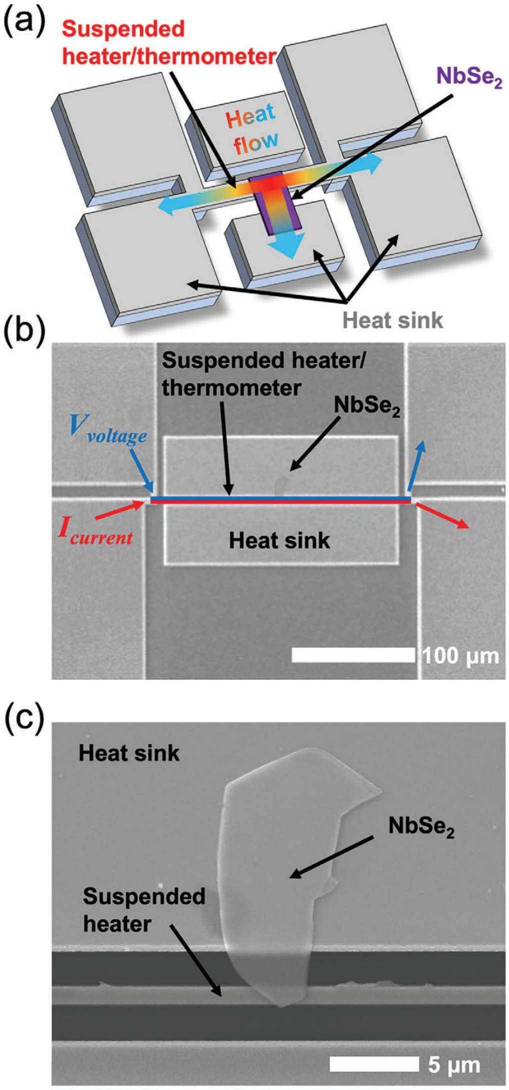

Figure 2. a) Schematic of T-bridge measurement setup. b) SEM image of the suspended heater and heat sink. c) SEM image of the sample placed on the heater and heat sink.

this measurement method its name, i.e., T-bridge method.[55] A micromanipulator was used to select and position a thin film sample onto the heater and heatsink for measurement. A small drop of ethanol was added onto the substrate to facilitate the transfer of the thin film by using the micromanipulator.[56] Once the sample was placed on the heater and heatsink, the ethanol was dried off with a blast of air. After the substrate was dried adequately, a field emission scanning electron microscope (FE-SEM, IT-500HR, JEOL) was used to measure the sample's dimensions and its location on the heater. The sample's thickness was measured with atomic force microscopy (AFM, NX-10, Park Systems).

The thermal conductivities of the as-prepared $NbSe_2$ samples were measured from 50 to 300 K by using the T-bridge method[55] (Figure 2b). In the T-bridge method, a sample, $NbSe_2$ in our case, is placed across a suspended heater and heat sink (Figure 2c). An electrical current is applied to the heater to increase the temperature on one side of the sample. This induces a heat flux from the sample to the heat sink. Additionally, the suspended heater acts as a thermometer, and by measuring the temperature difference between the two sides of the sample, its thermal conductivity can be determined. The thermal conductivity of a SiO_2 thin film was measured to verify our measurement setup (Figure S2, Supporting Information). The measured results showed that the thermal conductivity of the SiO_2 thin film measured using the T-bridge method agrees with the reference bulk data,[57] validating the T-bridge method.

3. Theoretical Analysis

3.1. Density Functional Theory Calculations

The theoretical framework of this study employs first-principles calculations based on density functional theory (DFT) using periodic boundary conditions. The calculations were performed using the Vienna Ab initio Simulation Package (VASP)[58,59] with the projector augmented wave (PAW) method.[60,61] The exchange-correlation interactions were treated using the Perdew–Burke–Ernzerhof (PBE)[62] functional within the generalized gradient approximation (GGA). A plane-wave basis set with a kinetic energy cutoff of 500 eV was utilized for expanding the Kohn–Sham orbitals. The calculations incorporated van der Waals (vdW) corrections through the DFT-D3 method with Becke-Johnson (BJ) damping.[63] A Γ-centered k-point mesh was generated using a 0.2 $Å^{-1}$ k-spacing, resulting in $11 \times 11 \times 3$ and $11 \times 11 \times 2$ grids for the 2H and 2H-3R phases, respectively. The structural optimization was performed with stringent convergence criteria, where the total energy convergence was set to 10^{-8} eV and the Hellmann–Feynman forces were minimized to less than 10^{-3} eV $Å^{-1}$. The space groups $P6_3/mmc$ (no. 194) and $P6_3mc$ (no. 186) were determined for the 2H and 2H-3R phases, respectively.

3.2. Phonon Dispersion and Scattering

The harmonic phonon calculations were performed using the finite-displacement method on a $6 \times 6 \times 1$ supercell with atomic displacements of 0.01 Å. For anharmonic interatomic force constants (IFCs), cutoff radii of 10 and 8 Bohr were applied for third-order and fourth-order IFCs, respectively, considering only up to three-body interaction terms. All IFC calculations were conducted using the ALAMODE[64] software, with data derived from ab initio molecular dynamics (AIMD) simulations at 300 K. These simulations were performed for 2500 steps with a 2 fs time step on a $6 \times 6 \times 1$ supercell using Γ-point sampling. After the initial 500 steps, 100 AIMD snapshots were extracted at intervals of 20 steps. To minimize cross-correlation among configurations, individual atoms in each snapshot were displaced by 0.1 Å in random orientations. The third-order and fourth-order IFCs were estimated using compressive sensing (Adaptive-LASSO[65]) with fourfold cross-validation applied to the sampled structures.

Furthermore, because the Grüneisen parameter is an indicator of the probability of phonon–phonon scattering, the

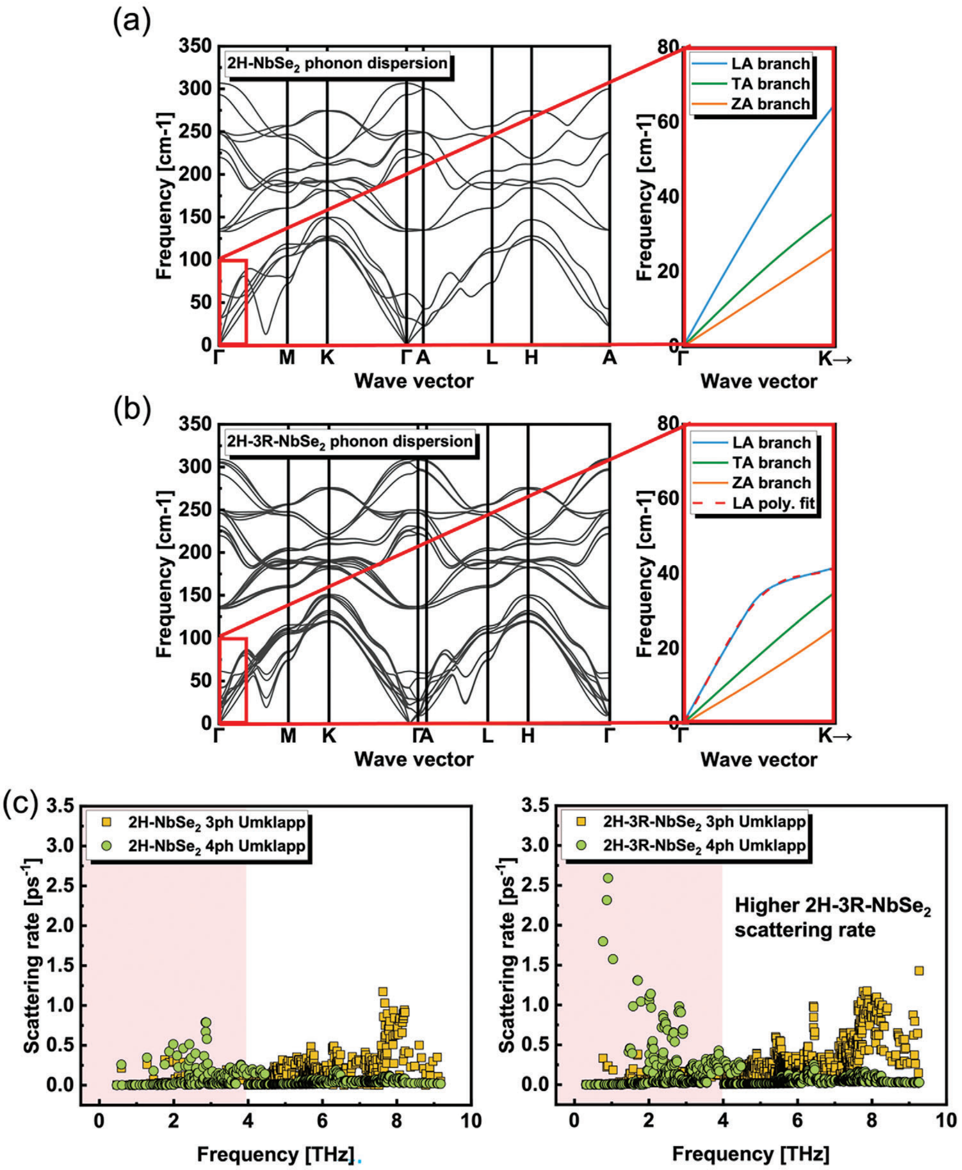

Figure 3. a) Phonon dispersion of 2H-NbSe$_2$ showing a linear relationship between phonon frequency and wave vector near the Γ point. b) 2H-3R-NbSe$_2$ phonon dispersion showing the nonlinear relationship between phonon frequency and wave vector near the Γ point, where the kink in the LA branch can be observed. c) 3 ph (yellow) and 4 ph (green) Umklapp scattering rates of 2H- (top) and 2H-3R-NbSe$_2$ (bottom). The red highlighted areas represent the stronger 4 ph scattering of 2H-3R-NbSe$_2$ than that of 2H-NbSe$_2$.

change in unit cell volume is expected to affect phonon–phonon scattering.[48,49] Temperature-renormalized harmonic force constants at 300 K were used to compute phonon group velocities and Grüneisen parameters, with cubic IFCs included for the latter. Scattering rates were calculated under the single-mode relaxation time approximation (SMRTA), accounting for three-phonon (3ph) and four-phonon (4ph) scattering processes via ShengBTE[66] and FourPhonon.[67] The self-consistent phonon (SCP) theory[64] was employed to obtain temperature-renormalized harmonic force constants, eliminating imaginary frequencies and ensuring more physically reliable phonon scattering calculations.[68]

4. Results and Discussion

As illustrated in Figure 1a, the STEM investigations unequivocally reveal that 2H-3R-NbSe$_2$ exhibits a repetitive stacking sequence comprising the A, B, C', and B' layers, whereas 2H-NbSe$_2$ is characterized by a simpler stacking sequence involving only the A and B' layers. Crucially, lattice constants derived from STEM and XRD analyses (Table 1) confirm that this variation in stacking configuration results in a 1.8-fold increase in the unit cell volume of 2H-3R-NbSe$_2$. A study by Chakraborty et al.[69] revealed that larger unit cells cause an increase in optical branches in phonon dispersion due to Brillouin zone folding. Such an effect leads to

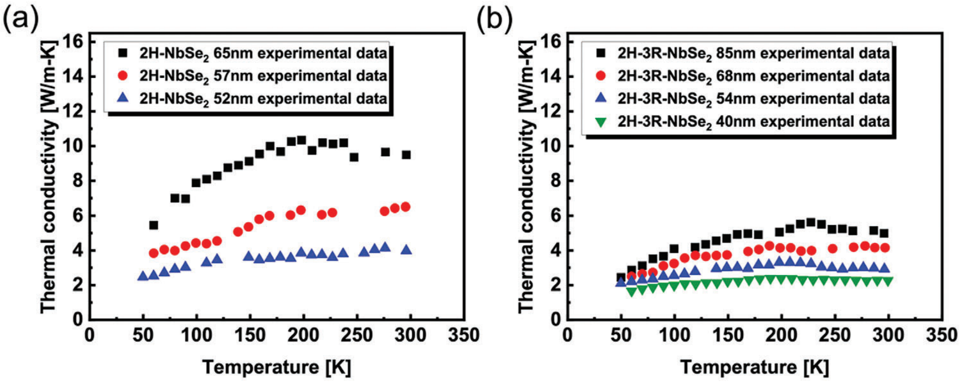

Figure 4. Measured total thermal conductivity of a) 2H-NbSe$_2$ and b) 2H-3R-NbSe$_2$.

reduced group velocity. Another work by Cui et al.[70] on silicon nanomeshes revealed that larger unit cells can reduce thermal conductivity by increasing phonon anharmonic scattering and reduced group velocity owing to the Brillouin zone folding. Similarly, Baer et al.[71] showed that while larger unit cells show reduced group velocity due to zone folding, the increase in phonon scattering shows a more dominant effect on the reduction of thermal conductivity. As such, the phonon dispersion of the 2H- and 2H-3R-NbSe$_2$ was investigated to study the effect of the unit cell size on the thermal conductivity of the two NbSe$_2$ polymorphs.

The phonon dispersion relationships of the 2H- and 2H-3R-NbSe$_2$ are shown in **Figure** 3a,b, respectively. Upon closer inspection of phonon dispersion near the Γ point (enlarged section in Figure 3b), the LA branch of the 2H-3R phase shows a kink, which results in a nonlinear relationship between the phonon frequency and wavevector. Therefore, while the phonon group velocity of the 2H phase was determined by linear Debye approximation, the group velocity of the 2H-3R phase was determined by nonlinear approximation.[72,73] The approximated phonon group velocities of 2H- and 2H-3R-NbSe$_2$ were 2108.42 and 1874.73 m s^{-1}, respectively. Phonon group velocity may alternatively be expressed as $v_g \sim v_s = \sqrt{E/\rho}$ where v_s is the velocity of sound, E is the elastic modulus, and ρ is the density. Clearly, a change in unit cell volume leads to a change in density, resulting in a variation in phonon group velocity, which is consistent with the difference relative to the phonon group velocity approximated from phonon dispersion. Additionally, compared to the unit cell of 2H-NbSe$_2$ which consists of six atoms, the enlarged unit cell of 2H-3R-NbSe$_2$ consists of 12 atoms. Consequently, 2H-NbSe$_2$ had 15 optical phonon branches, and this number increased to 33 for 2H-3R-NbSe$_2$. The increased number of optical phonon branches of 2H-3R-NbSe$_2$ indicated that thermal energy is absorbed rather than transported. However, as the number of acoustic phonon branches was three for both 2H- and 2H-3R-NbSe$_2$, energy transfer was limited. This effect may have reduced the phonon group velocity owing to increased inter-branch scattering.[46,47]

Table 2. Comparison of the experimentally measured total thermal conductivity of different materials and their polymorphs at 300 K.

Material	Polytype	Thermal conductivity [W m-K^{-1}]
Ge$_2$Sb$_2$Te$_5$[22]	h-GST	1.5
	c-GST	0.6
	a-GST	0.2
InAs[23]	WZ	14
	ZB	7.5
Cu$_2$SnS$_3$[24]	Ordered	1.03
	Disordered	0.45
NbSe$_2$ (This work)	2H	9.5
	2H-3R	4.2

The effect of the difference between the unit cell volumes of 2H- and 2H-3R-NbSe$_2$ on their respective thermal conductivities was further investigated by studying their phonon anharmonicity. Phonon anharmonicity was characterized using the Grüneisen parameter, $\gamma(\omega) = d(\ln \omega)/d(\ln V)$, where ω denotes the phonon frequency, and V is the unit cell volume.[41,43,48,49,74] The calculated Grüneisen parameter values were 1.28 and 1.44 for 2H-NbSe$_2$ and 2H-3R-NbSe$_2$, respectively. The effect of this difference in the Grüneisen parameter was observed in the phonon-phonon scattering rates. Figure 3c and Figure S3 (Supporting Information) depict the calculated Umklapp and normal scattering rates of the 3 and 4 ph of 2H- and 2H-3R-NbSe$_2$, respectively. Although the calculated normal scattering rates of 2H- and 2H-3R-NbSe$_2$ were similar, their Umklapp scattering rates were different. As can be seen in Figure 3c, the 3 ph scattering rates of 2H- and 2H-3R-NbSe$_2$ were similar, while the 4 ph Umklapp scattering rate of 2H-3R-NbSe$_2$ was considerably higher than that of 2H-NbSe$_2$ in the low-frequency range. Additionally, for the 2H- and 2H-3R phases, the 4 ph scattering rates were considerably higher in the low-frequency region than the 3 ph scattering rates. Therefore, 4 ph scattering must be considered when determining the thermal conductivities of these two NbSe$_2$ polymorphs. The phonon phase space was also investigated to study the effect of larger unit cells on the phonon scattering rates (Figure S4, Supporting Information). Furthermore, the calculated phonon scattering rates clearly highlighted that the larger and more complex unit cell of the 2H-3R phase increased the probability of phonon-phonon scattering and was expected to affect its thermal conductivity.

The total thermal conductivity of NbSe$_2$, as measured from 50 to 300 K by using the aforementioned T-bridge method, is depicted in **Figure** 4a,b. **Table** 2 shows the comparison of the measured total conductivity at 300 K of different materials and

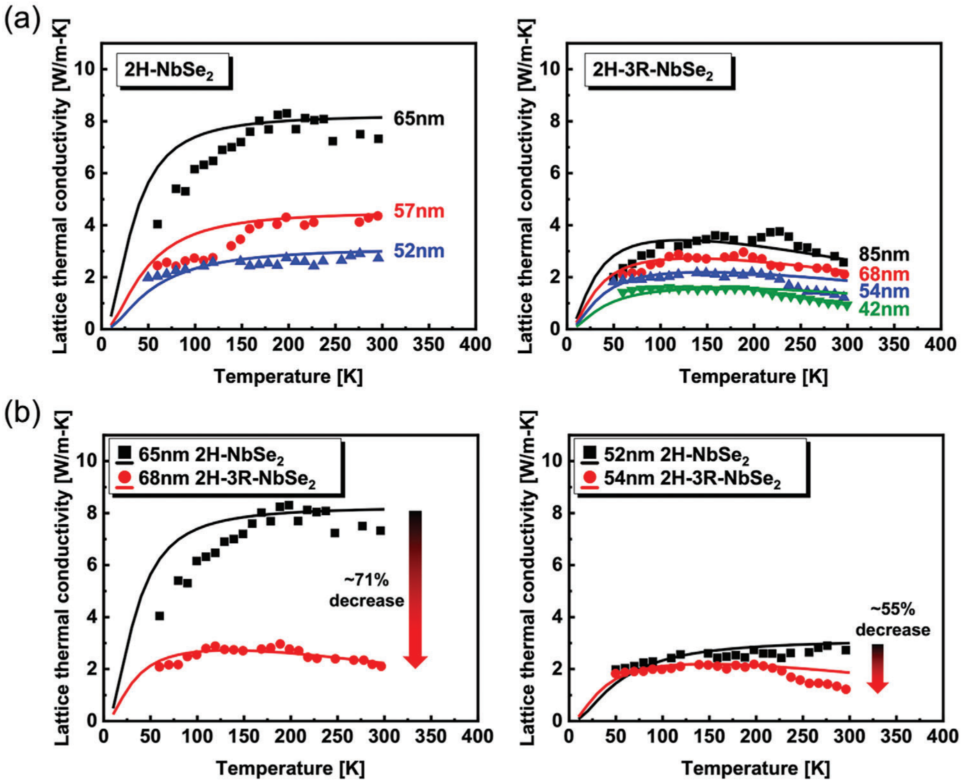

Figure 5. a) Measured lattice thermal conductivity of 2H-NbSe$_2$ and 2H-3R-NbSe$_2$ plotted against theoretically calculated values. b) Lattice thermal conductivities of 2H- and 2H-3R-NbSe$_2$ samples with similar thicknesses of ≈60 and 50 nm.

their polymorphs. The lattice thermal conductivities of 2H- and 2H-3R-NbSe$_2$ can be obtained by subtracting the electronic thermal conductivities from their measured total thermal conductivities. By using the Wiedemann–Franz law, the electronic thermal conductivities of 2H- and 2H-3R-NbSe$_2$ can be calculated from their electrical conductivities, as described in a previous study[45] and illustrated in Figure S5 (Supporting Information). At 300 K, the calculated electronic thermal conductivity of 2H-NbSe$_2$ was ≈1.5 W mK^{-1} while that of 2H-3R-NbSe$_2$ was ≈0.3 W mK^{-1}. According to the literature, the 2H phase NbSe$_2$ exhibits metallic behaviors.[45] The electronic thermal conductivity of pure metallic materials increases until a certain temperature and converges to a certain value. Therefore, the effect of electronic thermal conductivity must be considered when studying metallic materials such as 2H-NbSe$_2$. Unlike that of pure metals, the electronic thermal conductivity of alloys continues to increase with increasing temperature (see Figure S5, Supporting Information). According to previously calculated values, the electronic thermal conductivity of 2H-NbSe$_2$ is higher than that of 2H-3R-NbSe$_2$ at 300 K. Given that 2H-NbSe$_2$ is a metallic material, the effect of electronic thermal conductivity on its overall thermal conductivity is stronger, resulting in the formation of an increasing trend with temperature. By contrast, because the 2H-3R phase possesses semimetallic properties, its electronic thermal conductivity has a weaker effect than that of the 2H phase, resulting in the formation of a different trend. Additionally, as the effect of electronic thermal conductivity is weaker, the total thermal conductivity of the 2H-3R phase is lower than that of the 2H phase. According to the results, the lattice thermal conductivities of both 2H- and the 2H-3R-NbSe$_2$ decreased as the sample thickness decreased (see **Figure 5**a). However, there was a marginal difference in the thermal conductivity trend with increasing temperature. The thermal conductivity of the 2H phase tended to increase more rapidly with increasing temperature than that of the 2H-3R phase.

To calculate the lattice thermal conductivity of NbSe$_2$ in terms of temperature and thickness, the Callaway model was utilized by considering the normal and Umklapp scattering rates as the 3 and 4 ph scattering rates, along with the group velocities calculated from phonon dispersion (see Supplementary Information). The total scattering rate follows Matthiessen's rule, and is expressed as the sum of the individual scattering rates, as follows:

$$\frac{1}{\tau_c} = \frac{1}{\tau_N} + \frac{1}{\tau_U} + \frac{1}{\tau_{4ph}} + \frac{1}{\tau_B} \tag{1}$$

where τ_c, τ_N, τ_U, τ_{4ph}, and τ_B denote the combined, normal, Umklapp, 4 ph, and boundary scattering rates, respectively. The phonon scattering parameters used in the thermal conductivity calculation were derived from the previously calculated scattering rates (**Table 3**). The calculated lattice thermal conductivity was plotted along with the previously measured values, as depicted in Figure 5a. The calculated and measured thermal conductivities of 2H-NbSe$_2$ agree with each other, and thermal conductivity tends to increase continuously with temperature. Likewise, the calculated and measured thermal conductivities of

Table 3. Scattering parameters used in the Callaway model to calculate the lattice thermal conductivities of 2H- and 2H-3R-$NbSe_2$.

	B_N [s K^{-3}]	B_U [s K^{-1}]	B_{4ph} [s K^{-1}]
2H	5.09×10^{-48}	1.0×10^{-42}	5.75×10^{-46}
2H-3R	2.0×10^{-23}	8.0×10^{-23}	3.0×10^{-21}

2H-3R-$NbSe_2$ agree with each other. The thermal conductivities of both phases tended to decrease with decreasing thickness owing to an increase in boundary scattering. However, a comparison between the thermal conductivities of 2H- and 2H-3R-$NbSe_2$ indicates a difference in trends. Generally, the thermal conductivity of the 2H phase was greater than that of the 2H-3R phase. This difference was clearer when observing samples with thicknesses of approximately 60 nm and 50 nm (see Figure 5b). First, as can be seen from the previously calculated phonon dispersion relationship, the larger unit cell of the 2H-3R-$NbSe_2$ due to its complex stacking sequence led to an increase in the number of optical phonon branches. Additionally, there existed a kink in the LA branch of the 2H-3R-$NbSe_2$. These characteristics contributed to the reduction of the phonon group velocity, resulting in a lower value of 1874.73 m s^{-1} compared to the value of 2108.42 m s^{-1} for 2H-$NbSe_2$. This reduction in group velocity contributed toward lowering the thermal conductivity of 2H-3R-$NbSe_2$. Furthermore, the larger unit cell of 2H-3R-$NbSe_2$ affected the phonon selection rule and Grüneisen parameter, which are related to phonon-phonon scattering. A larger Grüneisen parameter of 1.44 was calculated for 2H-3R-$NbSe_2$ when compared to the value of 1.28 for 2H-$NbSe_2$. This difference in the Grüneisen parameter was reflected in the larger scattering rates of 2H-3R-$NbSe_2$, especially in terms of 4 ph Umklapp scattering. Additionally, the cumulative thermal conductivity was investigated (Figure S6, Supporting Information), revealing that for 2H-3R-$NbSe_2$ short mean free path phonons contribute significantly to the thermal conductivity. For 2H-$NbSe_2$, phonons with the mean free path in the range of ≈10 to 300 nm show great contribution to the thermal conductivity which agrees with the trend shown by other 2D layered materials such as MoS_2, $MoSe_2$, and WSe_2.[75] However, for the 2H-3R-$NbSe_2$, phonons in a shorter mean free path range of ≈10 to 60 nm contribute greatly to the thermal conductivity. This suggests that the thermal conductivity of 2H-3R-$NbSe_2$ is influenced by interlayer or intralayer defects such as differences in stacking sequence.[76–78] From these findings, it can be inferred that the lower group velocity and increased phonon-phonon scattering caused by the enlarged unit cell owing to the complex stacking sequence reduced the thermal conductivity of 2H-3R-$NbSe_2$ compared to that of 2H-$NbSe_2$. Bao et al.[79] observed this behavior for a similar 2D material, graphene. In the hexagonal (AAA), Bernal (ABA), and rhombohedral stacking sequences of graphene, the interatomic distances between the adjacent layers are different, leading to different electrical and thermal properties.

5. Conclusion

In this work, to study the difference in the thermal properties of a 2D layered material with different stacking orders, the thermal conductivities of the 2H and 2H-3R polymorphs of $NbSe_2$ were measured experimentally by using the T-bridge method and analyzed theoretically. The complex stacking sequence of 2H-3R-$NbSe_2$ resulted in a larger unit cell volume than that of 2H-$NbSe_2$. This effect reduced the acoustic phonon group velocity and enhanced the phonon scattering rates of 2H-3R-$NbSe_2$ compared to those of 2H-$NbSe_2$. Experimental results indicated that the 2H-3R phase had a lower thermal conductivity than that of the 2H phase owing to a lower group velocity and stronger Umklapp scattering. This difference in thermal conductivity between the two phases of $NbSe_2$ was verified based on the theoretical results obtained using the DFT-based Callaway model. The theoretical calculations confirmed that the lower thermal conductivity of 2H-3R-$NbSe_2$ was caused by the difference between the unit cell volumes of the two polymorphs, which was attributed to the reduced phonon group velocity and increased phonon scattering rate. Additionally, the thickness dependence of thermal conductivity owing to boundary scattering was observed. The differences in the thermal properties of the polymorphs of a single material reported herein can be used to guide the application of 2D materials and their polymorphs in thermal management devices.

Supporting Information

Supporting Information is available from the Wiley Online Library or from the author.

Acknowledgements

S.P., K.K., and K.K. contributed equally to this work. This work has been supported by the National Research Foundation of Korea (NRF) grant funded by the Korea government (MSIT) (NRF-2023R1A2C1005936 and NRF-2022M3C1A3091988).

Conflict of Interest

The authors declare no conflict of interest.

Data Availability Statement

Research data are not shared.

Keywords

niobium diselenide, polymorph, thermal conductivity, unit cell size

Received: September 30, 2024
Revised: December 23, 2024

[1] J.-P. Brog, C.-L. Chanez, A. Crochet, K. M. Fromm, *RSC Adv.* **2013**, *3*, 16905.
[2] Y. C. Liang, J. Yang, X. Yuan, W. J. Qiu, Z. Zhong, J. H. Yang, W. Q. Zhang, *Sci. Rep.* **2014**, *4*, 5063.
[3] M. Raya-Moreno, H. Aramberri, J. A. Seijas-Bellido, X. Cartoixà, R. Rurali, *Appl. Phys. Lett.* **2017**, *111*, 032107.

[4] H. F. Zhan, Y. Y. Zhang, J. M. Bell, Y. T. Gu, *J. Phys. D Appl. Phys.* **2014**, *47*, 015303.
[5] Y. Ding, B. Xiao, *Comput. Mater. Sci.* **2014**, *82*, 202.
[6] W. Li, N. Mingo, *J. Appl. Phys.* **2013**, *114*, 054307.
[7] H. Wang, Y. Zhou, Z.-Y. Zeng, Y. Cheng, Q.-F. Chen, *Solid State Commun.* **2019**, *293*, 40.
[8] V.-H. Chu, T.-H. Le, T.-T. Pham, D.-L. Nguyen, *RSC Adv.* **2023**, *13*, 4202.
[9] F. Eriksson, E. Fransson, C. Linderälv, Z. Fan, P. Erhart, *ACS Nano* **2023**, *17*, 25565.
[10] S. G. Wang, H. F. Feng, Z.-X. Guo, *Comput. Mater. Sci.* **2023**, *228*, 112345.
[11] H. Cao, Y. Luo, W. Jiao, W. Lei, S. Han, H. Liu, *Nanotechnol.* **2024**, *35*, 185702.
[12] E. H. L. Falcao, F. Wudl, *J. Chem. Technol. Biot.* **2007**, *82*, 524.
[13] A. A. Balandin, *Nat. Mater.* **2011**, *10*, 569.
[14] J. R. Olson, R. O. Pohl, J. W. Vandersande, A. Zoltan, T. R. Anthony, W. F. Banholzer, *Phys. Rev. B* **1993**, *47*, 14850.
[15] K. S. Novoselov, A. K. Geim, S. V. Morozov, D. Jiang, Y. Zhang, S. V. Dubonos, I. V. Grigorieva, A. A. Firsov, *Science* **2004**, *306*, 666.
[16] A. A. Balandin, S. Ghosh, W. Bao, I. Calizo, D. Teweldebrhan, F. Miao, C. N. Lau, *Nano Lett.* **2008**, *8*, 902.
[17] D. L. Nika, A. A. Balandin, *Thermal Transport in Graphene, Few-Layer Graphene and Graphene Nanoribbons*, Springer International Publishing, Switzerland, **2016**, pp. 339–363.
[18] P. Klemens, D. Pedraza, *Carbon* **1994**, *32*, 735.
[19] R. Taylor, *Philos. Mag.* **1966**, *13*, 157.
[20] P. Kim, L. Shi, A. Majumdar, P. L. McEuen, *Phys. Rev. Lett.* **2001**, *87*, 215502.
[21] C. Yu, L. Shi, Z. Yao, D. Li, A. Majumdar, *Nano Lett.* **2005**, *5*, 1842.
[22] Q. Li, O. Levit, E. Yalon, B. Sun, *J. Appl. Phys.* **2023**, *133*, 135105.
[23] F. Zhou, A. L. Moore, J. Bolinsson, A. Persson, L. Fröberg, M. T. Pettes, H. Kong, L. Rabenberg, P. Caroff, D. A. Stewart, N. Mingo, K. A. Dick, L. Samuelson, H. Linke, L. Shi, *Phys. Rev. B* **2011**, *83*, 205416.
[24] K. Lohani, H. Nautiyal, N. Ataollahi, C. Fanciulli, I. Sergueev, M. Etter, P. Scardi, *J. Phys. Chem. C* **2021**, *125*, 178.
[25] A. Splendiani, L. Sun, Y. Zhang, T. Li, J. Kim, C.-Y. Chim, G. Galli, F. Wang, *Nano Lett.* **2010**, *10*, 1271.
[26] G.-H. Lee, Y.-J. Yu, X. Cui, N. Petrone, C.-H. Lee, M. S. Choi, D.-Y. Lee, C. Lee, W. J. Yoo, K. Watanabe, *ACS Nano* **2013**, *7*, 7931.
[27] W. Choi, N. Choudhary, G. H. Han, J. Park, D. Akinwande, Y. H. Lee, *Mater. Today* **2017**, *20*, 116.
[28] N. D. Cultrara, Y. X. Wang, M. Q. Arguilla, M. R. Scudder, S. S. Jiang, W. Windl, S. Bobev, J. E. Goldberger, *Chem. Mater.* **2018**, *30*, 1335.
[29] K. A. N. Duerloo, E. J. Reed, *ACS Nano* **2016**, *10*, 289.
[30] S. S. Coutinho, M. S. Tavares, C. A. Barboza, N. F. Frazao, E. Moreira, D. L. Azevedo, *J. Phys. Chem. Solids* **2017**, *111*, 25.
[31] S. Li, F. C. Lei, X. Peng, R. Q. Wang, J. F. Xie, Y. P. Wu, D. S. Li, *Inorg. Chem.* **2020**, *59*, 11935.
[32] R. Sun, J. Deng, X. Wu, M. Hao, K. Ma, Y. Ma, C. Zhao, D. Meng, X. Ji, Y. Ding, Y. Pang, X. Qian, R. Yang, G. Li, Z. Li, L. Dai, T. Ying, H. zhao, S. Du, G. Li, S. Jin, X. Chen, *Nat. Commun.* **2023**, *14*, 6689.
[33] T. Zhu, P. M. Litwin, M. G. Rosul, D. Jessup, M. S. Akhanda, F. F. Tonni, S. Krylyuk, A. V. Davydov, P. Reinke, S. J. McDonnell, M. Zebarjadi, *Mater. Today Phys.* **2022**, *27*, 100789.
[34] V. I. Beletskii, O. A. Gavrenko, B. A. Merisov, M. A. Obolenskii, A. V. Sologubenko, G. Y. Khadjai, K. B. Chashka, *Low Temp. Phys.* **1998**, *24*, 273.
[35] S. Ghosh, W. Bao, D. L. Nika, S. Subrina, E. P. Pokatilov, C. N. Lau, A. A. Balandin, *Nat. Mater.* **2010**, *9*, 555.
[36] F. Roeske, H. R. Shanks, D. K. Finnemore, *Phys. Rev. B* **1977**, *16*, 3929.
[37] E. Boaknin, M. A. Tanatar, J. Paglione, D. Hawthorn, F. Ronning, R. W. Hill, M. Sutherland, L. Taillefer, J. Sonier, S. M. Hayden, J. W. Brill, *Phys. Rev. Lett.* **2003**, *90*, 117003.
[38] Z. Zhang, Y. Jiao, S. K. S. Saravana Karthikeyan, S. G. Ramaraj, F. Zhang, N. Nguyen Dang, X. Qin, X. Liu, *J. Phys. Chem. C* **2023**, *127*, 17213.
[39] P. Erhart, P. Hyldgaard, D. O. Lindroth, *Chem. Mater.* **2015**, *27*, 5511.
[40] B. Mortazavi, T. Rabczuk, *RSC Adv.* **2017**, *7*, 11135.
[41] X. F. Yan, B. W. Wang, Y. L. Hai, D. R. Kripalani, Q. Q. Ke, Y. Q. Cai, *Sci. China Phys. Mech.* **2022**, *65*, 117004.
[42] C. Q. Yu, Y. X. Hu, J. He, S. Lu, D. F. Li, J. Chen, *Appl. Phys. Lett.* **2022**, *120*, 132201.
[43] J. P. Heremans, *Nat. Phys.* **2015**, *11*, 990.
[44] H. Eidsvåg, M. Rasukkannu, D. Velauthapillai, P. Vajeeston, *RSC Adv.* **2021**, *11*, 3759.
[45] H. Moon, J. Kim, J. Bang, S. Hong, S. Youn, H. Shin, J. W. Roh, W. Shim, W. Lee, *Nano Energy* **2020**, *78*, 105197.
[46] W. Kim, *J. Mater. Chem. C* **2015**, *3*, 10336.
[47] H. Kim, G. Park, S. Park, W. Kim, *ACS Nano* **2021**, *15*, 2182.
[48] D. T. Morelli, V. Jovovic, J. P. Heremans, *Phys. Rev. Lett.* **2008**, *101*, 035901.
[49] A. M. Hofmeister, H.-k. Mao, *Proc. Natl. Acad. Sci* **2002**, *99*, 559.
[50] E. Chen, W. Xu, J. Chen, J. H. Warner, *Mater. Today Adv.* **2020**, *7*, 100076.
[51] M. S. Sokolikova, P. C. Sherrell, P. Palczynski, V. L. Bemmer, C. Mattevi, *Nat. Commun.* **2019**, *10*, 712.
[52] P. Phalswal, P. K. Khanna, H.-G. Rubahn, Y. K. Mishra, *Mater. Adv.* **2022**, *3*, 5672.
[53] S. F. Meyer, R. E. Howard, G. R. Stewart, J. V. Acrivos, T. H. Geballe, *J. Chem. Phys.* **1975**, *62*, 4411.
[54] Á. Coogan, Y. K. Gun'ko, *Mater. Adv.* **2021**, *2*, 146.
[55] J. Kim, D. J. Seo, H. Park, H. Kim, H. J. Choi, W. Kim, *Rev. Sci. Instrum.* **2017**, *88*, 054902.
[56] X. Yang, X. Q. Li, Y. Deng, Y. X. Wang, G. L. Liu, C. Wei, H. Li, Z. Wu, Q. H. Zheng, Z. W. Chen, Q. Jiang, H. M. Lu, J. Zhu, *Adv. Funct. Mater.* **2019**, *29*.
[57] D. G. Cahill, *Rev. Sci. Instrum.* **1990**, *61*, 802.
[58] G. Kresse, J. Furthmüller, *Comput. Mater. Sci.* **1996**, *6*, 15.
[59] G. Kresse, J. Furthmüller, *Phys. Rev. B* **1996**, *54*, 11169.
[60] P. E. Blöchl, *Phys. Rev. B* **1994**, *50*, 17953.
[61] G. Kresse, D. Joubert, *Phys. Rev. B* **1999**, *59*, 1758.
[62] J. P. Perdew, K. Burke, M. Ernzerhof, *Phys. Rev. Lett.* **1996**, *77*, 3865.
[63] S. Grimme, S. Ehrlich, L. Goerigk, *J. Comput. Chem.* **2011**, *32*, 1456.
[64] T. Tadano, S. Tsuneyuki, *Phys. Rev. B* **2015**, *92*, 054301.
[65] H. Zou, *J. Am. Stat. Assoc.* **2006**, *101*, 1418.
[66] W. Li, J. Carrete, N. A. Katcho, N. Mingo, *Comput. Phys. Commun.* **2014**, *185*, 1747.
[67] Z. Han, X. Yang, W. Li, T. Feng, X. Ruan, *Comput. Phys. Commun.* **2022**, *270*, 108179.
[68] K. Kim, W. Hwang, S.-H. V. Oh, A. Soon, *Npj Comput. Mater.* **2023**, *9*, 154.
[69] P. Chakraborty, G. Xiong, L. Cao, Y. Wang, *Carbon* **2018**, *139*, 85.
[70] H. Cui, T. Maranets, T. Ma, Y. Wang, *Phys. Rev. B* **2024**, *110*, 075301.
[71] B. Baer, D. G. Walker, L. Lindsay, *Phys. Rev. B* **2024**, *109*, 104310.
[72] J. D. Chung, A. J. H. McGaughey, M. Kaviany, *J. Heat Trans-T. Asme* **2004**, *126*, 376.
[73] M. Schrade, T. G. Finstad, *Phys. Status Solidi B* **2018**, *255*, 1800208.
[74] Y. Zhang, E. Skoug, J. Cain, V. Ozoliņš, D. Morelli, C. Wolverton, *Phys. Rev. B* **2012**, *85*, 054306.
[75] M. Zulfiqar, Y. Zhao, G. Li, Z. Li, J. Ni, *Sci. Rep.* **2019**, *9*, 4571.
[76] D. Aketo, T. Shiga, J. Shiomi, *Appl. Phys. Lett.* **2014**, *105*, 131901.
[77] A. N. Gandi, U. Schwingenschlögl, *Europhys. Lett.* **2016**, *113*, 36002.
[78] A. Shafique, A. Samad, Y.-H. Shin, *Phys. Chem. Chem. Phys.* **2017**, *19*, 20677.
[79] C. Bao, W. Yao, E. Wang, C. Chen, J. Avila, M. C. Asensio, S. Zhou, *Nano Lett.* **2017**, *17*, 1564.